

Effect of droplet shrinking on surface acoustic wave response in microfluidic applications

Bui, Thu Hang; Nguyen, Van; Vollebregt, Sten; Morana, Bruno; van Zeijl, Henk; Chu Duc, Trinh ; Sarro, Pasqualina M.

DOI

[10.1016/j.apsusc.2017.07.140](https://doi.org/10.1016/j.apsusc.2017.07.140)

Publication date

2017

Document Version

Accepted author manuscript

Published in

Applied Surface Science

Citation (APA)

Bui, T. H., Nguyen, V., Vollebregt, S., Morana, B., van Zeijl, H., Chu Duc, T., & Sarro, P. M. (2017). Effect of droplet shrinking on surface acoustic wave response in microfluidic applications. *Applied Surface Science*, 426, 253-261. <https://doi.org/10.1016/j.apsusc.2017.07.140>

Important note

To cite this publication, please use the final published version (if applicable).
Please check the document version above.

Copyright

Other than for strictly personal use, it is not permitted to download, forward or distribute the text or part of it, without the consent of the author(s) and/or copyright holder(s), unless the work is under an open content license such as Creative Commons.

Takedown policy

Please contact us and provide details if you believe this document breaches copyrights.
We will remove access to the work immediately and investigate your claim.

Effect of Droplet Shrinking on Surface Acoustic Wave Response in Microfluidic Applications

ThuHang Bui^{1,2,a}, Van Nguyen³, Sten Vollebregt¹, Bruno Morana¹, Henk van Zeijl¹, Trinh Chu Duc², and Pasqualina M. Sarro¹

¹Microelectronics, Delft University of Technology, Delft, 2628 BX, The Netherlands

²Electronics and Telecommunications, University of Engineering and Technology, VNU-HN, Hanoi, Vietnam

³Graduate School of Information Science, Tohoku University, Japan

Abstract. The effect of the contact angle and radius of a microsize droplet on the surface acoustic wave (SAW) response for microfluidic applications is reported. It is studied through the dynamic change of the droplet shape during the evaporation process. An aluminium nitride SAW device, operating at 125.7 MHz, is utilized to investigate the deformation of the droplet shape (contact angle and contact radius) caused by shrinking. The large cavity placed on the propagation path distorts the in-band SAW response one time at the centre frequency. The fractional coefficient of the SAW insertion loss, before and after dropping the liquid on the propagation path, is continuously recorded. The change in the fractional coefficient shows that the radiated acoustic kinetic energy depends on the contact area between the sessile micro-size droplet and the SAW device more than the contact angle of the droplet. Three droplet volumes have been considered, namely 0.05, 0.1 and 0.13 μl , and the electrical results show a better agreement with the theoretical data than the optical image data. The average duration of the fractional coefficient change for these cases is 420, 573 and 760 seconds, respectively. The effect of the hydrophobicity versus hydrophilicity of the contact surface on the duration of the fractional coefficient change is studied by coating the SAW with a silicon oxide or hexamethyldisilazane (HMDS) thin layer. For the same 0.05 μl sessile droplet on the hydrophobic surface, this duration is on average 110 seconds longer than that on the hydrophilic surface.

1. Introduction

The leakage phenomenon of surface acoustic waves (SAWs) into a liquid forms a significant limitation for the employment of SAW devices in liquid applications. If we consider the unlimited ambient liquid medium on the propagation path of a SAW device, most of the SAW energy is emitted into the liquid medium^{[1]-[2]}. This emitted energy is related to a longitudinal component of the SAWs which is referred to as compressional waves, Rayleigh surface acoustic waves, or longitudinal waves^{[3]-[5]}. In practice, when the liquid medium has an insignificant volume (less than a microliter) like a small droplet, the emitted kinetic energy can transport and manipulate fluids such as separating, trapping, driving, mixing, jetting and atomizing^{[6]-[8]}. Diverse mechanisms, such as microfluidic sensor, actuation and manipulation of the micro-objects have been studied^{[7]-[10]}. Depending on the envisioned SAW microfluidic applications, the applied power and operating frequency need to be determined. For example, the centre frequency of the SAW fluid actuation and manipulation at microscale can be in the range of 0.01 – 1000 MHz. Low input power (in the order of mWatts) generates a preliminary acoustic streaming on the free surface of the sessile droplet for vibration, mixture, driving applications while higher input power (from 1 Watt) leads to breakup of the stabilizing interface of the sessile droplet^{[11]-[12]}.

^a Email: t.h.bui@tudelft.nl

For a micro-size sessile droplet, typical phenomena in the sensor, actuation and manipulation are acoustic streaming flow, acoustic radiation force, jetting phenomenon which are influenced by the formation of the droplet on the surface. Besides, an evaporation phenomenon plays a crucial role in microfluidic SAW applications owing to the presence of the changeable contact angle and area between the liquid and the piezoelectric substrate in the short transient time [8], [10], [13]. One obvious aspect of the droplet evaporation is an unstable and turning-back SAW response during and after the short duration of the evaporation duration. Therefore, the shrinking sessile droplet placed on the propagation path can have a relevant effect on the microfluidic-actuation and -manipulation applications of the SAW device. The presence of adjacent energy from the liquid-solid interface is influenced by the behaviour of the droplet (surface tension, density, contact area and shrinking droplet shape) [14] and the properties of the piezoelectric device (surface wettability, surface roughness, input power and centre frequency) [7]-[8].

This paper reports on the effect of the change of the droplet volume, through the contact angle and radius, on the SAW device response. The theoretical analysis shows that the shrinking behaviour of both the contact angle and radius during the droplet evaporation process influences the variation duration of the SAW response. This is expressed by the fractional coefficient of the SAW response before and after dropping liquid on the propagation path of the SAW device. The slow or fast attenuation duration of the fractional coefficient depends on the variation of the contact angle, radius or both at the same time. It is also caused by the fluid-structural solid interface due to the presence of the pinning force relative to the change in contact angle. Besides, as the surface property affects the droplet evaporation process and the contact area region between the liquid and the piezoelectric medium, it also influences the duration of the variation of the SAW response.

2. Fundamentals of the Rayleigh SAW in liquid domain

In Snell's law on the refraction phenomenon, the incidence angle of the denser medium must be smaller than the critical angle at the contact to avoid the probable total internal reflection. For a piezoelectric medium, the Rayleigh angle in the forward medium is considered. For example, the longitudinal component of the SAW is radiated into the less dense medium at the Rayleigh angle [15]. In order to have the refraction phenomenon at the contact surface between piezoelectric and less dense medium like liquid, or gas, the contact angle of the less dense medium should be larger than Rayleigh angle.

2.1. Attenuation into the ambient constant liquid

For a refraction phenomenon, a wave is radiated from the denser medium to the less dense one. Rayleigh surface acoustic waves are emitted at the Rayleigh angle because the sound of speed in the liquid is much smaller than that of the longitudinal waves [5], [16]. This refracted angle in the liquid medium is calculated by [17]:

$$\sin(\theta_R) = \frac{v_f}{v_R} = \frac{\lambda_f}{\lambda} \quad (1)$$

where v_f , λ_f are the velocity and wavelength of the liquid; while v_R and λ are related to the piezoelectric material. At the contact surface of the piezoelectric material, the amplitude of the normal particle displacement is at a maximum and is equal to that in the liquid medium [16], [17]. For a liquid medium with rectangle-shape domain $V_l(a, b, \lambda)$, the average SAW energy is transported from the contact surface to a maximum depth (up to λ) and to a width b because its energy concentrates mostly on the surface and can spread below the surface up to one [5] or a few wavelengths [18]. For an ideal, homogenous and isotropic piezoelectric surface, the fractional coefficient is calculated by:

$$\alpha \sim \frac{ba}{b\lambda} \frac{\rho_f v_f}{\rho v_R} \quad (2)$$

where ρ , ρ_f and a are the piezoelectric density, the liquid density and the length of the liquid medium, respectively. The attenuation of the SAW beam into each micrometre length of the liquid domain is expressed by α/a [dB/ μm]. This attenuation depends on the properties of the liquid and piezoelectric material (density, sound speed and wavelength) considered.

2.2. Attenuation into the droplet-shape domain

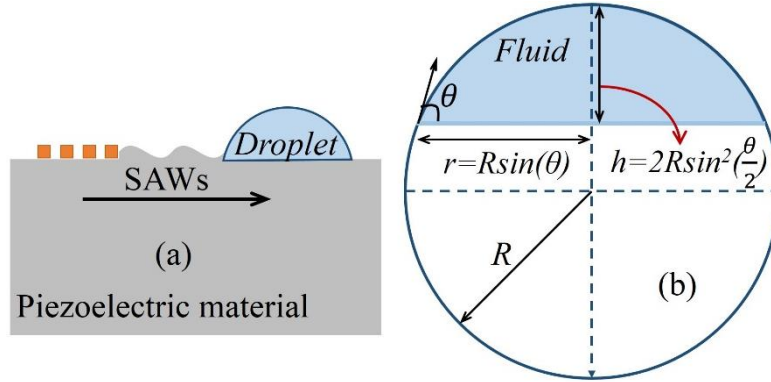


Fig. 1. (a) The typical SAW-based microfluidic and (b) the geometrical parameters of the zoomed-in 2D droplet view.

If we considered a microliter droplet, the droplet height is much smaller than the liquid wavelength (See Fig. 1a). However, it becomes a dynamic medium due to the evaporation process. For example, if the considered droplet has a height h , a contact radius r and a contact angle θ as shown in Fig. 1b, the liquid volume V_0 is then given by:

$$V_0 = \frac{\pi}{3} r^3 \frac{\sin \theta (2 + \cos \theta)}{(1 + \cos \theta)^2} \quad (3)$$

As the above fractional coefficient is relative to the space domain $V_1(2r, 2r, \lambda) = 4r^2\lambda$, the fractional coefficient for the sessile droplet with a volume V_0 is rewritten as:

$$\alpha(r, \theta) \sim \left(\frac{\pi}{6} \frac{\rho_f v_f}{\lambda^2 \rho v_R} \right) r^2 \frac{\sin \theta (2 + \cos \theta)}{(1 + \cos \theta)^2} \sim kr^2 \frac{\sin \theta (2 + \cos \theta)}{(1 + \cos \theta)^2} \quad (4)$$

with the condition $\pi > \theta > 0$.

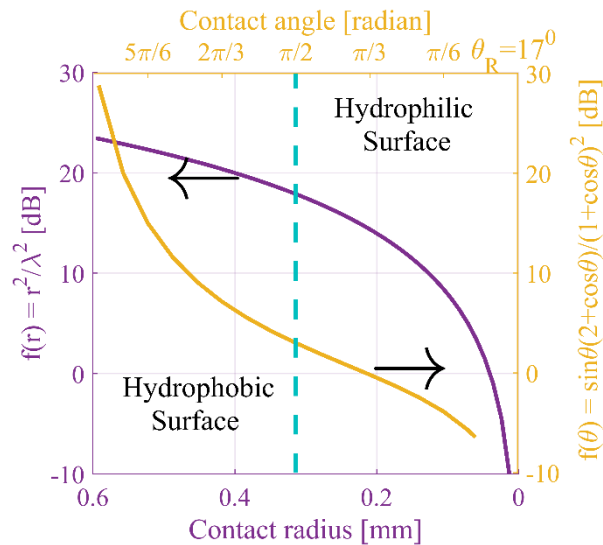


Fig. 2. The fractional coefficient corresponding to the variation of the contact angle and radius of the droplet on a hydrophilic ($\theta_0 < 90^\circ$) and hydrophobic ($\theta_0 \geq 90^\circ$) surface.

The fractional coefficient depends on the variation of the contact radius and contact angle during the evaporation process. The variation of the fractional coefficient in the shrinking contact angle case is slower than that in the shrinking contact radius as shown in Fig. 2, especially for a hydrophilic surface ($\theta < 90^\circ$). Averagely, for a 1-mm decrease of the contact radius, the descending velocity equals 4.39 times that of the 1-radian decrease of the contact angle. The variation of the contact angle can be neglected for hydrophilic and super-hydrophilic surface ($\theta_R < \theta < 90^\circ$) when the droplet volume decreases mainly due to the contact radius change^[14].

3. Emission of the SAW energy in the evolving micro-droplet

During the evaporation process of the sessile droplet, the domain of the liquid medium varies continuously because of the shrinking contact angle, radius and height. Therefore, the measured insertion loss changes during the evaporation process. To analyse this variation, the evolution of the droplet in the time domain and the variable fractional coefficient of the lost energy are considered.

3.1. The evolution of the droplet

The evolution of the droplet is a variation of the contact radius and contact angle to reach a quasi-equilibrium shape at the transient instance. This variation is due to one or two parameters. If only the contact radius changes, it is called as a constant contact angle (CA) mode and if only the contact angle change, it is a constant contact radius (CR) mode. If both parameters change, it is a stick-slide mode (SS) mode^[19]. Based on the rate of the mass loss reported by Popov^{[20]-[22]}, the time derivative equation for any contact angle and radius is:

$$\frac{1}{g(\theta)f(\theta)} \frac{dr^2}{dt} + \frac{r^2}{(1+\cos\theta)^2 f(\theta)} \frac{d\theta}{dt} = \frac{D(c_s - c_\infty)}{\rho_f} \quad (6)$$

where $f(\theta) = \frac{\sin\theta}{1+\cos\theta} + 4 \int_0^\infty \frac{1+\cosh 2\theta\tau}{\sinh 2\pi\tau} \tanh[(\pi-\theta)\tau] d\tau$ is a function of the variable θ and

$$g(\theta) = \frac{\sin^3\theta}{(1-\cos\theta)^2(2+\cos\theta)}$$

with c_s , c_∞ and D being the saturation concentration, the ambient concentration and the diffusion coefficient of the liquid vapour in the atmosphere, respectively^[20]. When the evaporation process is on a hydrophilic surface and under a homogeneous environment, the most commonly reported form is a serial order of three modes, CR ($r = r_0$ and $\theta = \theta_0 \rightarrow \theta_1^*$), SS ($r = r_0 \rightarrow r_1$ and $\theta = \theta_1^* \rightarrow \theta_2^*$) and CA ($r = r_1 \rightarrow 0$ and $\theta = \theta_2^*$)^{[22]-[23]}. Sometimes, it is simplified into two modes (CR and CA) as shown in Fig. 3.

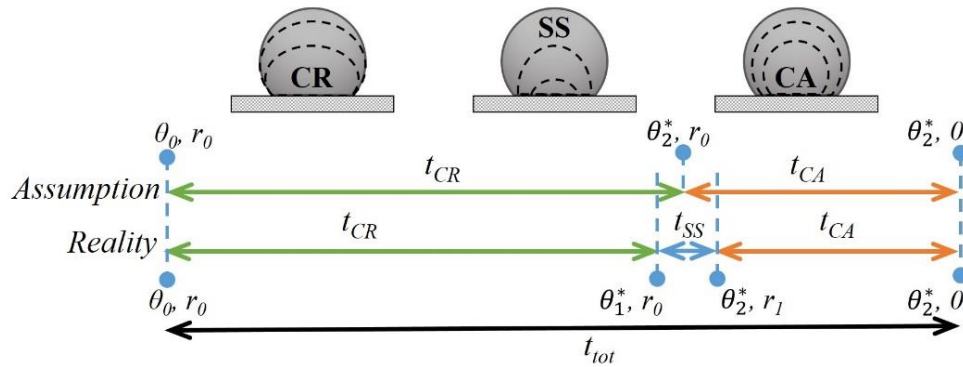


Fig. 3. The lifetime of the common real and assumed droplet evaporation process on the hydrophilic surface.

The lifetime of the liquid evaporation process t_{tot} is the total of three modes (like $t_{tot} = t_{CR} + t_{SS} + t_{CA}$) when $\theta = \theta_0 \rightarrow \theta_2^*$ and $r = r_0 \rightarrow 0$. It can be simplified as the lifetime of the droplet evaporation which includes only CA ($\theta = \theta_0 \rightarrow \theta_2^*$, $r = r_0$) and CR ($\theta = \theta_2^*$, $r = r_0 \rightarrow 0$) modes; thus the total time is calculated as:

$$t_{tot} = \int_{\theta_2^*}^{\theta_0} \frac{\rho_f r_0^2}{D(c_s - c_\infty)(1 + \cos \theta)^2 f(\theta)} d\theta + \frac{\rho_f r_0^2}{2D(c_s - c_\infty)g(\theta_2^*)f(\theta_2^*)} \quad (7)$$

For the CR mode, the contact angle recedes from $\theta = \theta_0$ to $\theta = \theta_1^*$, from Eq. 6, the duration of a droplet evaporating and the contact angle are calculated by:

$$t_{CR} = \int_{\theta_1^*}^{\theta_0} \frac{\rho_f r_0^2}{D(c_s - c_\infty)(1 + \cos \theta)^2 f(\theta)} d\theta \quad (8)$$

For the CA mode ($\theta = \theta_2^*$ and $r = r_1 \rightarrow 0$), the change in the contact radius leads to a decrease of the liquid volume. These duration and contact radius are rewritten as:

$$t_{CA} = \frac{\rho_f r_1^2}{2D(c_s - c_\infty)g(\theta_2^*)f(\theta_2^*)} \quad (9)$$

For the SS mode, $\theta(t)$, $r(t)$ decrease and the volume reduces until the contact angle reaches the minimum contact angle θ_2^* ($\theta_R \leq \theta_2^* \leq \theta_1^* \leq \theta_0$) and the contact radius reaches r_1 . The duration for the SS mode is t_{SS} .

$$t_{SS} = \int_{\theta_2^*}^{\theta_1^*} \frac{\rho_f r_0^2}{D(c_s - c_\infty)(1 + \cos \theta)^2 f(\theta)} d\theta + \frac{\rho_f (r_0^2 - r_1^2)}{2D(c_s - c_\infty)g(\theta_2^*)f(\theta_2^*)} \quad (10)$$

The relationship among θ_0 , θ_1^* and θ_2^* is based on the unbalanced surface tension or unbalanced Young's force. It is reported and determined by the maximum pinning force f_p which is a ratio of the practical pinning force at the reachable minimum angle and the preliminary pinning force at the initial angle. It depends on surface roughness, substrate-fluid interface and the constant surface tensions of the fluid vapour^[19]. The contact angle θ shrinks until it reaches $\theta = \arccos(f_p + \cos \theta_0)$ with f_p in the range of $(0, 2)$ ^[19]. For the CR mode, the contact angle with the maximum pinning force $f_{p,1}$ varies until it reaches the critical contact angle $\theta_1^* = \arccos(f_{p,1} + \cos(\theta_0))$ with the condition $0 < f_{p,1} \leq 1 - \cos \theta_0$. For the SS mode, the contact angle corresponding to $f_{p,2}$ continues to vary until a new minimum critical contact angle $\theta_2^* = \arccos(f_{p,2} + \cos(\theta_1))$. The duration of the CR mode depends on the first pinning force $f_{p,1}$ while that of the SS mode depends on the second pinning force $f_{p,2}$. The condition $0 < f_{p,1} + f_{p,2} \leq 1 - \cos \theta_0$ has to be satisfied because θ_1^* and θ_2^* are real numbers.

The pinning force ratio $\frac{f_{p,2}}{f_{p,1}}$ depends on the hydrophilic or hydrophobic characteristic of the contact surface, the liquid properties (like surface tension and density), the contact area of the liquid on the surface and the environment. Some values of the maximum pinning forces ($f_{p,1}$; $f_{p,2}$) are shown in Fig. 4.

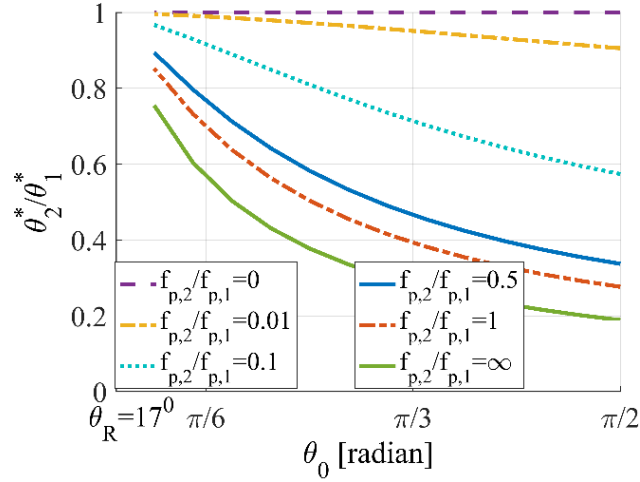


Fig. 4. The dependence of the critical contact angle ratio $\frac{\theta_2^*}{\theta_1^*}$ on the initial contact angle corresponding to various values of the pinning forces.

The smaller the ratio is, the shorter the SS mode occurs. For the super-hydrophobic surface corresponding to the infinitely small values of this ratio, only two distinct modes (CR and CA) appear, corresponding to $f_{p,2} = 0$. When the angle ratio θ_2^* / θ_1^* approaches to one, the pinning force ratio $f_{p,2}$ is close to zero and the duration of the SS mode goes to zero. In case, the pinning force ratio goes to infinite or the first pinning force equals zero ($f_{p,1} = 0$), only SS and CA modes happen. When the second pinning force $f_{p,2}$ is larger than the first one $f_{p,1}$, the angle ratio θ_2^* / θ_1^* always lies in the small range bounded by the red ($f_{p,2}/f_{p,1} = 1$) and green ($f_{p,2}/f_{p,1} = \infty$) line. It also means that the SS mode lasts longer.

3.2. Attenuation of the SAW emission into the dynamic microdroplet formation

For the hydrophilic surface, the evaporation process normally has three modes, thus the fractional coefficient varies through three modes. From the above equations (Eqs. 4, 8), (Eqs. 4, 9) and (Eqs. 4, 10), the fractional coefficient of the SAW energy emission in the CR, SS, CA modes is calculated (simply referred to as CR, SS, CA modes for brevity). In the whole dynamic microdroplet evaporation process, it is rewritten as:

$$\alpha(t) = \alpha_{CR(t=0 \rightarrow t_{CR})} + \alpha_{SS(t=t_{CR} \rightarrow t_{CR}+t_{SS})} + \alpha_{CA(t=t_{CR}+t_{SS} \rightarrow t_{CR}+t_{SS}+t_{CA})} \quad (11)$$

The attenuation duration of each mode is relative to the evaporation time of the droplet. For example, all probable cases of the droplet evaporation process are shown in Fig. 5a, and the corresponding attenuation behaviours of the fractional coefficient are reported in Fig. 5b. The CR mode takes place more quickly than the other modes while the CA mode is the slowest one. The fractional coefficient in the CA mode reduces slightly at first and then considerably at the end. It is relative to the physical behaviour of the dramatically shrinking contact radius in the end of the droplet evaporation process. Fig. 5 also shows that the droplet volume is affected by the descending contact angle whereas the faster attenuation of the fractional coefficient is caused by the shrinking contact radius in the CA mode. The slope of the fractional coefficient is similar when the CR and SS mode in the droplet evaporation happens. The shrinking of the sessile droplet in the CR and SS modes leads to a slow attenuation duration of the fractional coefficient, while in the CA mode, it causes fast attenuation duration.

The values of the pinning forces ($f_{p,1}$; $f_{p,2}$) are also shown in Fig. 5b. If the total pinning forces are generally similar, the total evaporation duration is similar, thus the variation duration of the fractional

coefficient is mostly equal (for example, CR-SS, SS and CR-SS-CA case; CR-CA and SS-CA case). If the total pinning forces is small, it leads to a long evaporation process and variation duration of the fractional coefficient. For example, the CA case ($f_{p,1} = f_{p,2} = 0$) is the longest case whereas the CR case ($f_{p,1} + f_{p,2} = 0.04$) is the shortest case.

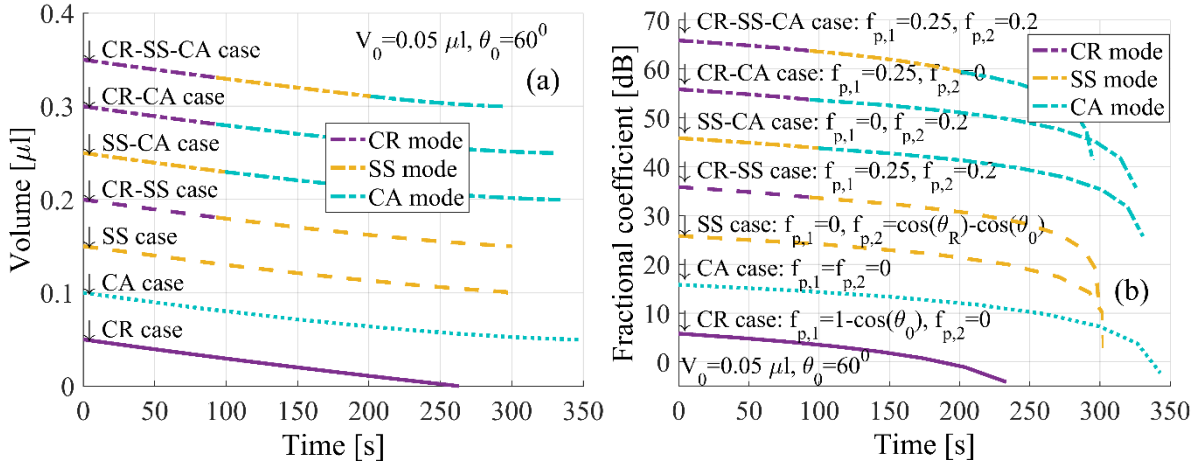


Fig. 5. (a) Evolution with time of the droplet volume during the evaporation sequence and (b) fractional coefficient of the SAW response in all probable modes (10 dB and $0.05 \mu\text{l}$ offset in Y axis has been added to separate (a) the fractional coefficients and (b) the volume in modes).

Fig. 6a shows the variation of the fractional coefficient corresponding to different initial contact angles. For the hydrophilic surface, the smaller the initial contact angle is, the shorter the CR and SS modes are, whereas the longer the CA mode is. For the hydrophobic surface, if the initial contact angle is larger, the CR mode is shorter, whereas the SS and CA modes are longer. The total attenuation duration of the fractional coefficient is also longer. When the CR and SS modes are simplified into the CR mode, the attenuation duration of the fractional coefficients in the same initial contact angle ($\theta_0 = 60^\circ$) are approximately similar. If the surface of the liquid-solid interface is hydrophobic ($\theta_0 > 90^\circ$), the variation duration of the SAW response is longer than that on the hydrophilic surface ($\theta_0 \leq 90^\circ$).

In practical, the values θ_1^* and θ_2^* can be simplified into a single value if there is a little change in the contact radius in the SS mode on the hydrophilic surface. For example, the radius reduces only to 95 % in the SS mode of the CR-SS-CA case and the simplified CR-CA case in Fig. 6a. On the superhydrophobic surface, only the CA and CR mode exist^[13]. The transformation duration from θ_1^* to θ_2^* sometimes occurs quickly, especially for a liquid having a high evaporation rate and weak surface tension (for example: acetone, ethanol, isopropyl alcohol)^{[14]-[24]} or for the hydrophobic surface^{[13], [22]}. These angles depend on the characteristic of the substrate surface, the liquid, the ambient atmosphere. Note that the case $\theta_1^* = \theta_2^*$, it is a common example for the droplet evaporation process on the superhydrophobic surface including two modes (CA and CR mode).

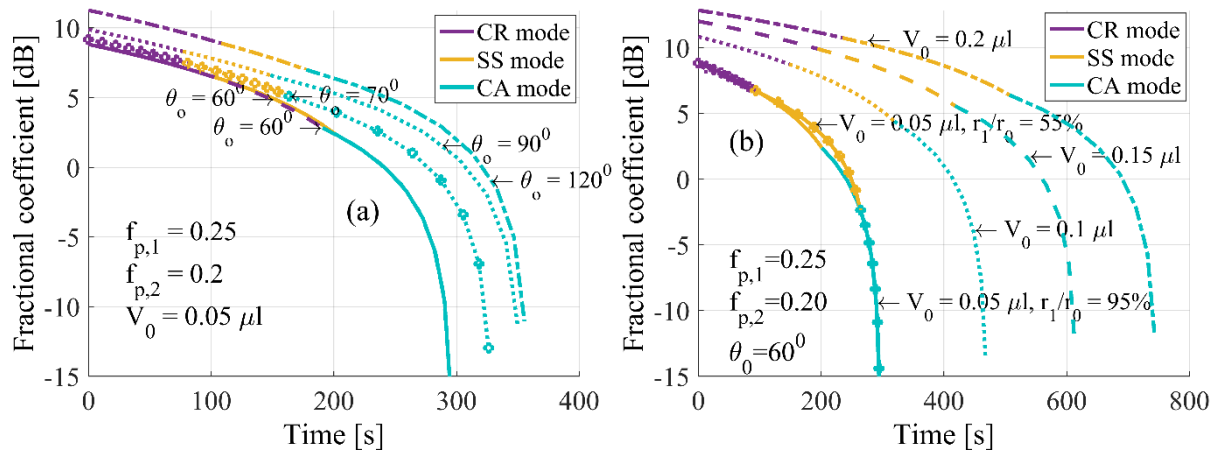


Fig. 6. (a) Fractional coefficient corresponding to various values of the initial contact angle, namely 60° , 90° , and 120° , respectively. (b) Various ascending values of the initial volume $V_0 = 0.05, 0.1, 0.13$ and $0.2 \mu\text{l}$; $r_1/r_0 = 95\%$ and the spinning forces $(f_{p,1}; f_{p,2}) = (0.25; 0.20)$.

The droplet volume also causes the variation of the fractional coefficient (Fig. 6b). If the physical parameters (for example, pinning forces, and contact angle) change, all modes get affected. The attenuation duration of the fractional coefficient in the CR, SS, CA modes is longer, namely 55, 118 and 174 seconds if the droplet volume increases from 0.05 to 0.1 μl . It means that the larger the droplet volume placed in the propagation path is, the longer the variation of the insertion loss S_{21} lasts. The SS mode in the droplet evaporation process depends not only on the second pinning force $f_{p,2}$ but also on the contact radius decrease ($r = r_0 \rightarrow r_1$). It can occur longer and affect the slope of the fractional coefficient more if the decrease of the contact radius is larger as shown in Fig. 6b. For the 95 % decrease of the shrinking contact radius in the SS mode, the whole attenuation duration of the fractional coefficient is constant but in the CA mode is more sloping. Consequently, the variation duration of the SAW response is caused by the surface properties (expressed by the total of the pinning forces and initial contact angle) and the liquid properties (expressed by volume, density, sound velocity, evaporation rate and surface tension). The physical shrinking of the contact angle and radius in the CR, SS and CA mode in the droplet evaporation rate is the cause of the small and fast slope of the fractional coefficient.

4. Device fabrication and testing setup

4.1. SAW device with the hydrophilic surface

Although SAWs may be generated upon the surface of various piezoelectric materials such as quartz, lithium niobate, zinc oxide, PZT, here a CMOS compatible material, aluminium nitride thin film, is chosen. The fabrication procedure for the SAW device includes two main parts, namely patterning the interdigital transducer (IDT) fingers on a 1 μm aluminium nitride (AlN) thin film and two top-surfaces (one hydrophilic and one hydrophobic surface).

For the 125.7 MHz SAW device, a 50- Ω IDT impedance requires an acoustic aperture of 50 wavelengths^[5]. The IDTs of 40 straight electrode pairs are patterned by the optical photolithography on a silicon nitride (SiN) layer (Fig. 7a), added to protect the piezoelectric surface during the inductively coupled plasma-reactive ion etching. More detail on the fabrication process can be found in previous work^[24].

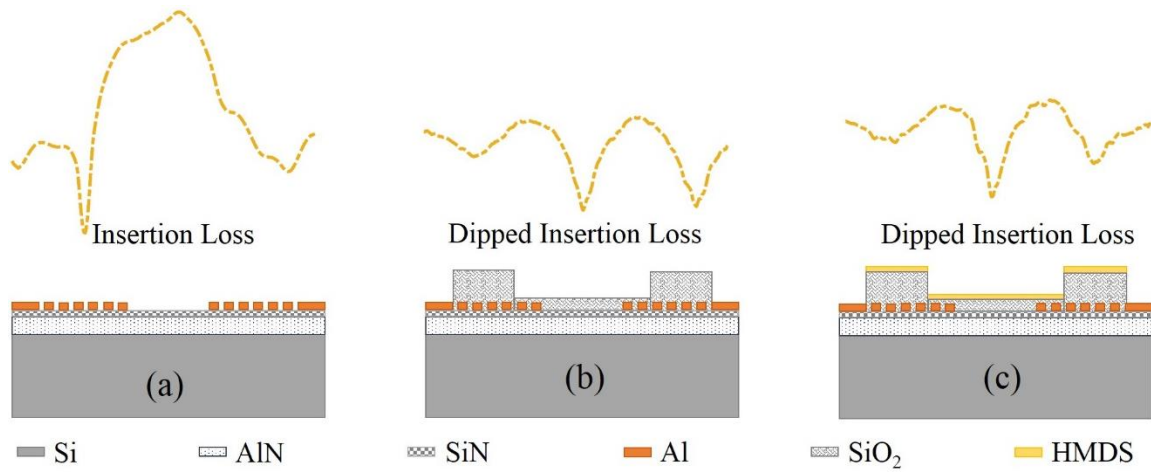


Fig. 7. (a) Conventional and experimental SAW structure with the typical and dipped insertion loss caused by (b) the SiO₂ and (c) HMDS thin-film cavity.

The hydrophilic surface used in the experiments is a **6.9 μm-thick** silicon oxide (SiO₂) thin film, deposited by PECVD (Fig. 7b). A cavity of 2 mm x 2.5 mm is created in the oxide to form a dip at the centre of the band. This means that the in-band response is distorted one time at the centre frequency as shown in the comparison of the conventional and dipped insertion loss of Fig. 7. For the conventional SAW device, the insertion loss after dropping the liquid varies around the primary insertion loss measured before dropping the liquid^[24]. For the dipped SAW device, the variation of the insertion loss after dropping stays at one side of the primary insertion loss. Hence, this variation during the shrinking process of the droplet is easier to observe. To increase the contact angle of the sessile droplet, a thin layer (**a few monolayers**) hexamethyldisilazane (HMDS) is coated by exposing the surface of the sample to its vapour for 15 minutes in the controller oven. The insertion loss before liquid dropping of the SAW device covered by HMDS is similar to that of the SAW device with only the SiO₂ thin film (Fig. 7b, c).

4.2. Measurement setup

The scattering matrix data of the SAW device is measured by **HP 8753E RF vector network analyzer** and collected continuously every 10 seconds by using the Cascade Microtech software. The applied power (5dBm) is small enough to influence insignificantly the evaporation process. The droplet is applied with the pipette PR2. The measurements are performed in a closed chamber to keep a stable measurement environment. The experiments are also performed in a controlled laboratory environment (**humidity 68 ± 2 % and temperature 19 ± 0.5 °C**) so to have a controlled evaporation process.

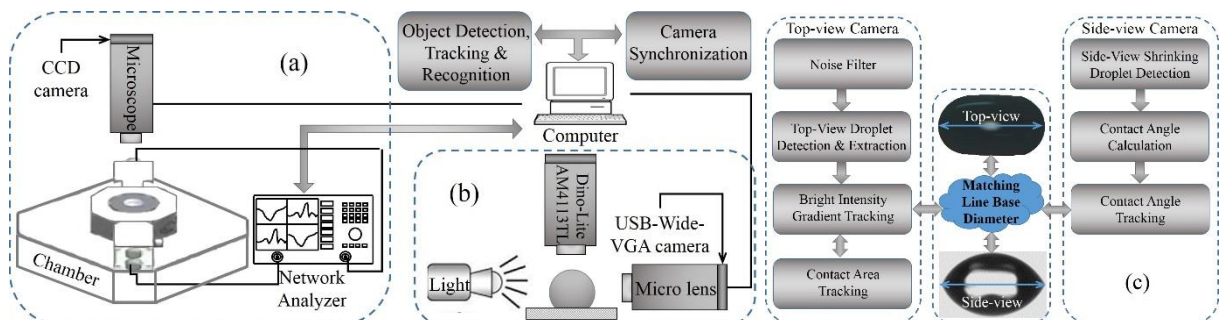


Fig. 8. Measurement setup for (a) the electrical data and the contact area, (b) the contact angle, and (c) camera synchronization algorithm.

Deionized water (DW) with a volume in the range of 0.05 – 0.13 μl is used in the experiments. This volume is selected to study the lower limit of detection of our SAW device and to avoid overflow from the cavity to the electrical contacts to take place. The droplet evaporation process is tracked by a top-view camera as shown in Fig. 8a. The contact radius and the bright intensity are recorded by this camera. The propagation path is a calibration for measuring the droplet contact area, width and length. The top-view optical images, collected by the CCD camera in Fig. 8a, are converted into grayscale images and their salt-and-pepper noise is filtered. Before processing the image, the ambient background of the droplet is removed. The brightness intensity of the spot is related to the number of pixels with the grey intensity smaller than the threshold. The threshold is adaptive to the average threshold of the individual optical image and ranges from 35 to 90 because of the automatic focus mode of the recorded video. The contact area is limited by the boundary black pixels.

The second system has a top-view and a side-view camera (Fig. 8b). The contact angle, temperature, line base diameter are recorded and measured by the contact angle system OCA20. The DINO top-view camera recorded initial optical images which are compared to those of the CCD top-view camera. The optical images of the top-view and CCD side-view cameras are synchronized by the line base diameter during the droplet evaporation process (see Fig. 8c).

As an example, data for the droplet volume of 0.13 μl are reported in TABLE I. The data extracted from the top-view optical images is processed to remove noise and background before contact area, length and width of the sessile droplet are measured. The contact angle is found after the synchronization of the side-view and top-view cameras. The initial data of the optical images, such as contact angle θ_0 , droplet volume V_0 , are used for the theoretical data. The variation of the contact angle is also considered and possibly anticipated by the bright intensity of the droplet which is processed by the optical images of the top-view camera. Based on the optical image data, the fractional coefficient

is approximately rewritten as $\alpha(s, \theta) \sim \frac{s}{\lambda^2} \frac{\sin \theta (2 + \cos \theta)}{(1 + \cos \theta)^2} \frac{\pi \rho_f v_f}{6 \rho v_R}$ where s is the contact area of the sessile droplet at time t .

TABLE I. Matching line base diameters of the synchronized cameras for the 0.13 μl sessile droplet case.

Time (seconds)	Top-view camera			Side-view camera
	Contact Area S (mm^2)	Length L (mm)	Width W (mm)	Contact Angle ($^\circ$)
0	1.31647	1.52419	1	65.5
100	1.30187	1.51210	0.991935	57.0
200	1.2992	1.47984	0.983871	49.1
300	1.29834	1.47984	0.983871	39.6
400	1.29761	1.47984	0.983871	26.7
500	1.29709	1.47581	0.983871	19.0
600	1.29619	1.47581	0.983871	17.5
700	1.04996	1.21774	0.9717740	16.8
730	0.0036583	0.201613	0.0322581	16.7
750	0	0	0	0

5. Results and discussions

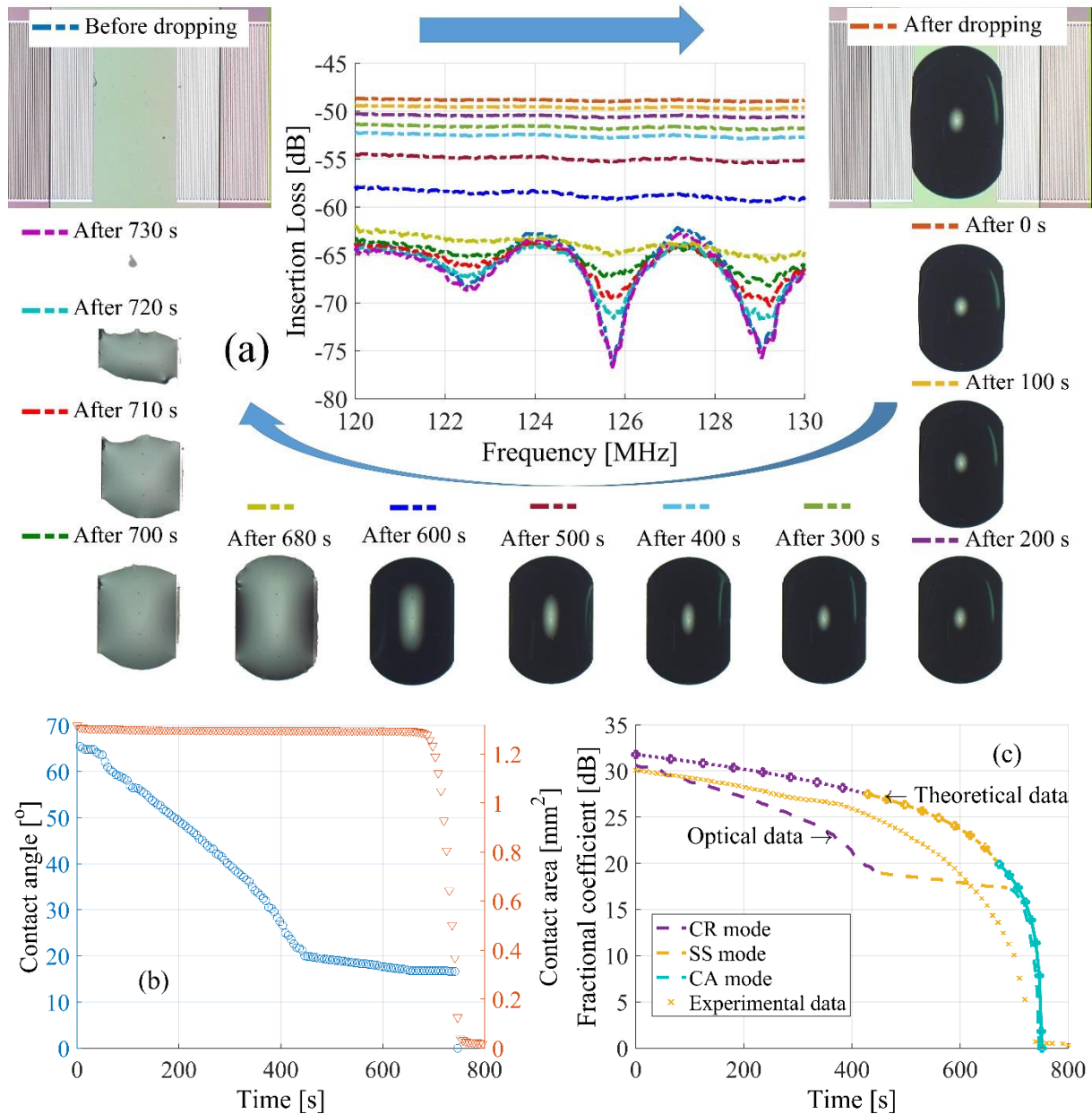


Fig. 9. (a) The variation of the insertion loss and the optical images from the top-view camera at several times of the $0.13 \mu\text{l}$ droplet on the hydrophilic surface. (b) The contact angle and radius change during the evaporation process of the sessile droplet recorded by the top-view camera. (c) Comparison of the variation of the fractional coefficient calculated using the theoretical data, optical-image data and electrical data.

The data from the top-view optical image and the corresponding SAW response are shown in Fig. 9a. In the first 450 seconds, the contact area of the sessile droplet (1.45 % evaporated contact area) is mostly constant, thus the insertion loss changes insignificantly. We refer to this situation as the CR mode which has a constant radius and changeable contact angle (from 65.5° down to 20.0°). This contact angle change can also be observed by the bright spot on the optical images, caused by the reflected light of the top-view microscope. The SS mode is a little stronger receding from 450 to 680 seconds because there are more 3.07 % reduced contact area and insignificantly reduced contact angle (from 20.0° down to 16.7°). During the first 680 seconds, corresponding to 4.52 % reduced contact area, the intensity of the bright spots changes continuously because of the changeable contact angle. Afterwards, the colour observation of the bright intensity of the sessile droplet shows that the contact

angle is mostly constant while the contact radius changes quickly. Here, the insertion loss starts to have a small fluctuation and then quickly returns to the initial status.

The parameters of the deionized water for the theoretical data are based on physical properties, and specific conditions as indicated in TABLE II.

TABLE II. Parameters of the sessile droplet used for the theoretical data

	Value	Unit
Diffusion coefficient D at 20°C	22.56×10^{-6}	m^2/s
Saturated vapor concentration c_s	0.015	kg/m^3
Initial contact angle θ_0	66	$^\circ$
Spinning force $f_{p,1}$	0.447	
Spinning force $f_{p,2}$	0.125	
Radius ratio (r_1/r_0)	95%	

Fig. 9c shows that the measured electrical data are in better agreement with the theoretical data than the optical image data. The reason is that the automatic focus mode of the top-view camera can produce small nonlinear values of the contact area. A pseudo-increase error is eliminated by the nonlinear filtering using the comparison of the contiguous values. However, errors caused by the pseudo-decrease values or the synchronization process of the top-view and side-view cameras can still occur. It is a limitation of the optical image processing.

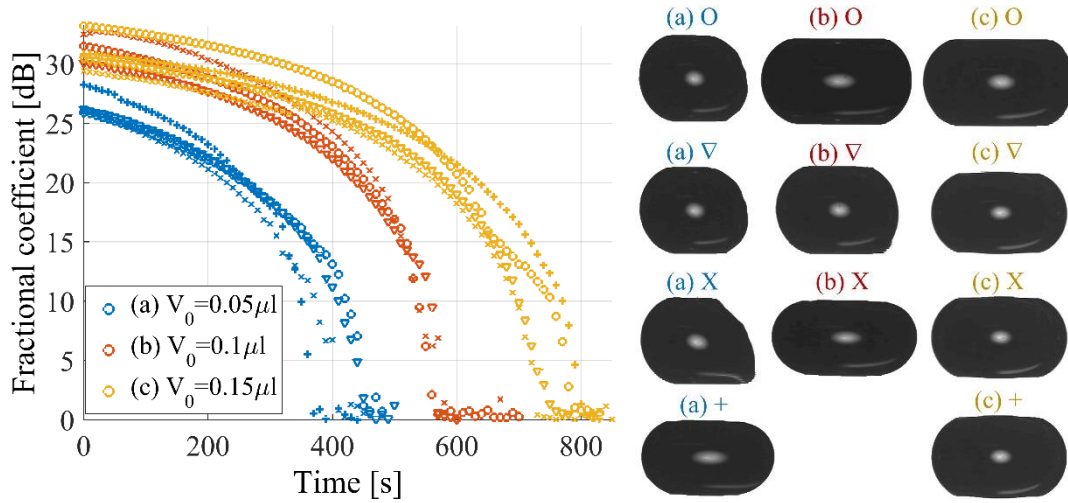


Fig. 10. The scatter plot of the variation of the fractional coefficient in the time domain when deionized water is dropped on the hydrophilic SAW surface (O, X, ∇, + from different experiments; blue scatters for the volume of $0.05 \mu\text{l}$, red ones for the volume of $0.1 \mu\text{l}$ and yellow ones for the volume of $0.13 \mu\text{l}$). (a), (b), (c) Optical images from the top-view camera corresponding to the droplet volume of 0.05 , 0.10 and $0.13 \mu\text{l}$.

The bright intensity observed by the top-view camera show the droplet evaporation experiences the CA-SS-CR mode sequence and at the end, the dramatic drop is related to the shrinking contact radius of the CR mode. The evaporation time of the same size droplet on the hydrophobic is longer than that on the hydrophilic surface^{[13]Error! Reference source not found.} because the pinning forces are larger. It means the variation duration of the contact angle can last longer. Similarly, if two droplets of the same volume but with the different contact angle and area are placed on the same surface, the one with the larger contact area evaporates faster because of the smaller pinning forces. The droplet keeps a similar shape as the contact area until the contact angle reaches a critical value θ_2^* . For a $0.05 \mu\text{l}$ droplet on the same hydrophilic surface, as the initial contact area of the sessile droplet (see image (a) + in Fig. 10) is

1.41 times that of the droplet (see image (a) O in Fig. 10), and its initial contact angle is smaller, its evaporation time is faster. Therefore, the fractional coefficient returns to zero more quickly. Fig. 10 also shows that the evaporation duration of the bigger droplet volume results in longer duration of the fractional coefficient variation, namely 420, 573 and 760 seconds for 0.05, 0.1, 0.13 μl . It is caused by the longer duration of the shrinking contact angle when the bigger droplet evaporates on the propagation path of the SAW device. In all cases, the fast attenuation of the fractional coefficient is caused by the dramatically descent of the contact radius in the droplet evaporation process.

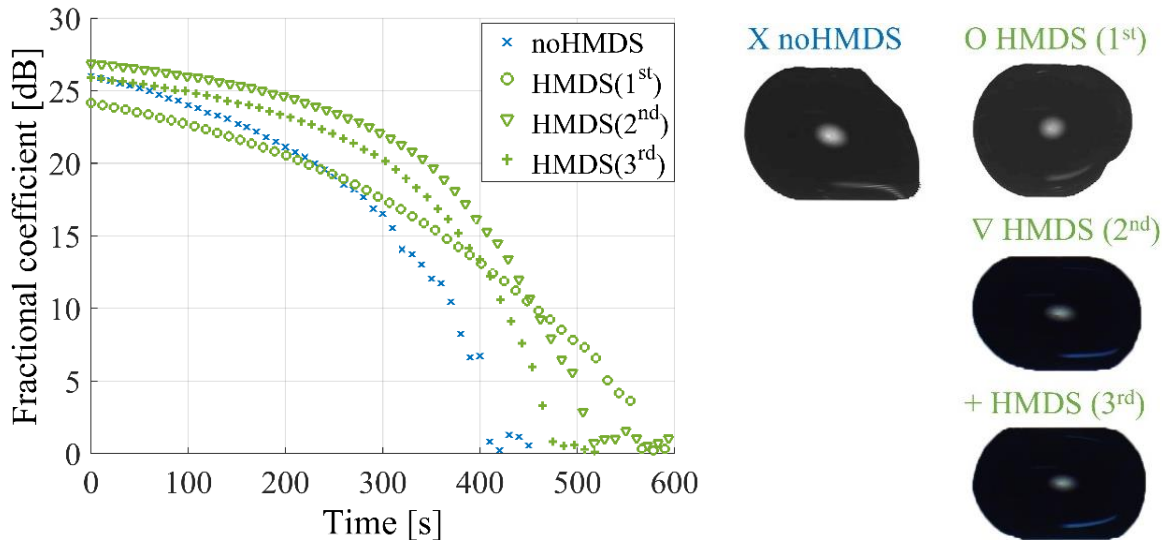


Fig. 11. The variation of the fractional coefficient during the 0.05 μl droplet evaporation on the hydrophobic (HMDS) and hydrophilic (no HMDS) surface of the SAW device.

In Fig. 11, results related to the same-volume droplet on the hydrophilic ($\theta < 90^\circ$ because of the silicon oxide film) and hydrophobic surface ($\theta > 90^\circ$ because of the HMDS layer) are shown. The contact angle of the droplet on the hydrophobic surface is larger because this contact area is smaller (91% to 98% contact area of the sessile droplet on the hydrophilic surface). The magnitude of the bright spot on the CCD top-view optical image shows the larger initial contact angle on the hydrophobic surface (O, ∇ and +). The droplet evaporation time is influenced by the contact angle because if the contact angle is smaller, the contact area is larger and the liquid layer is thinner. The saturation vapour pressure at the droplet surface is increased. The pinning force of the hydrophilic surface becomes smaller, the pinning time becomes longer; thus the evaporation time is shorter^{[13], [25]}. It is in good agreement with the measured time variation of the fractional coefficient for the hydrophilic and hydrophobic surface (average 110 seconds then on the HMDS layer).

6. Conclusions

The energy emitted into the liquid medium is different for the dissimilar contact area between the sessile droplet and the piezoelectric material. In additions, the evaporation phenomenon of the sessile droplet contributes as well. The dynamic change caused by the contact angle and radius of the sessile droplet occurs during the evaporation process. The change in contact radius influences the insertion loss more than the change in contact angle, especially on hydrophilic and super-hydrophilic surfaces ($\theta < 90^\circ$). The variation duration of the fractional coefficient is proportional to the droplet volume and the surface wettability. For example, it is 420, 573 and 760 seconds for the 0.05, 0.10 and 0.13 μl sessile droplet respectively, on the top hydrophilic film (SiO_2 film) of the SAW device. In average, it is 110 seconds longer if the droplet is placed on the hydrophobic layer (HMDS) compared to the hydrophilic layer (SiO_2). This work highlights the need to include, for proper use of SAW devices in microfluidic applications, the shape of the droplet on the surface, the effect of the evaporation phenomenon, droplet

volume and surface wettability, especially for the long-time actuation and manipulation in experiments.

7. Acknowledgements

The authors would like to acknowledge the support of Dr. Rene Poelma and Tom Scholtes at EKL lab, Dr. Atef Akhnoukh at Electronics Research lab of the Delft University of Technology, Dr. An Tran at Advanced Institute for Science and Technology, Hanoi University of Science and Technology and Dr. Catalin V. Rusu from the Computer Science Department at Babes-Bolyai University.

This work is partly supported by a Vietnamese Government scholarship.

8. References

- [1] S. Showko, K. Jun, Surface Acoustic Wave Sensors. *Japanese Journal of Applied Physics* **43**, 2799 (2004).
- [2] S. Tamura, R. E. Vines, J. P. Wolfe, Effects of liquid loading on surface acoustic waves in solids. *Physical Review B* **54**, 5151-5163 (1996).
- [3] Clemens C. W. Ruppel, T. A. Fjeldly, *Advances in Surface Acoustic Wave Technology, Systems and Applications*. (World Scientific, 2001), vol. 2.
- [4] S.V. Biryukov, Y.V. Gulyaev, V. Krylov, V. Plessky, *Surface Acoustic Waves in Inhomogeneous Media*. (Springer-Verlag Berlin Heidelberg New York, 1995), vol. 20.
- [5] J. Ballantine *et al.*, *Acoustic Wave Sensors, 1st Edition: Theory, Design, & Physico-Chemical Applications*. (ACADEMIC PRESS, USA, 1997).
- [6] A. Qi, L. Y. Yeo, J. R. Friend, Interfacial destabilization and atomization driven by surface acoustic waves. *Physics of Fluids* **20**, 074103 (2008).
- [7] R. Raghavan, J. Friend, L. Yeo, Particle concentration via acoustically driven microcentrifugation: microPIV flow visualization and numerical modelling studies. *Microfluid Nanofluid* **8**, 73-84 (2010).
- [8] M. K. Tan, J. R. Friend, L. Y. Yeo, Microparticle collection and concentration via a miniature surface acoustic wave device. *Lab on a Chip* **7**, 618-625 (2007).
- [9] G. Destgeer, H. J. Sung, Recent advances in microfluidic actuation and micro-object manipulation via surface acoustic waves. *Lab on a Chip* **15**, 2722-2738 (2015).
- [10] S. U. Senveli and O. Tigli, "Finite element method analysis of surface acoustic wave devices with microcavities for detection of liquids," *Journal of Applied Physics*, vol. 114, pp. -, 2013.
- [11] C. Witte, J. Reboud, R. Wilson, J. M. Cooper, S. L. Neale, Microfluidic resonant cavities enable acoustophoresis on a disposable superstrate. *Lab on a Chip* **14**, 4277-4283 (2014).
- [12] L. Y. Yeo, J. R. Friend, Ultrafast microfluidics using surface acoustic waves. *Biomicrofluidics* **3**, 012002 (2009).
- [13] D. H. Shin, S. H. Lee, J.-Y. Jung, J. Y. Yoo, Evaporating characteristics of sessile droplet on hydrophobic and hydrophilic surfaces. *Microelectronic Engineering* **86**, 1350-1353 (2009).
- [14] T. Bui, B. Morana, A. Akhnoukh, T. Chu Duc, P. M. Sarro, Liquid identification by using a micro-electro-mechanical interdigital transducer. *Analyst*, (2017).
- [15] S. Showko, M. Yoshikazu, M. Toyosaka, Experimental Study on Liquid Streaming by SAW. *Japanese Journal of Applied Physics* **28**, 126 (1989).
- [16] D. Morgan, *Surface Acoustic Wave Filters: With Applications to Electronic Communications and Signal Processing*. (Elsevier Ltd., ed. 2nd, 2007).
- [17] K. Dransfeld, E. Salzmann, in *Physical Acoustics*, W.P. Mason, R. N. Thurston, Eds. (Academic press, New York, 1970), Vol. VII, pp. 219-272.
- [18] L. Y. Yeo, J. R. Friend, Surface Acoustic Wave Microfluidics. *Annual Review of Fluid Mechanics* **46**, 379-406 (2014).
- [19] J. M. Stauber, S. K. Wilson, B. R. Duffy, K. Sefiane, On the lifetimes of evaporating droplets with related initial and receding contact angles. *Physics of Fluids* **27**, 122101 (2015).

- [20] Y. O. Popov, Evaporative deposition patterns: Spatial dimensions of the deposit. *Physical Review E* **71**, 036313 (2005).
- [21] S. Dash, S. V. Garimella, Droplet Evaporation Dynamics on a Superhydrophobic Surface with Negligible Hysteresis. *Langmuir* **29**, 10785-10795 (2013).
- [22] G. McHale, S. Aqil, N. J. Shirtcliffe, M. I. Newton, H. Y. Erbil, Analysis of Droplet Evaporation on a Superhydrophobic Surface. *Langmuir* **21**, 11053-11060 (2005).
- [23] T. A. H. Nguyen *et al.*, Theoretical and experimental analysis of droplet evaporation on solid surfaces. *Chemical Engineering Science* **69**, 522-529 (2012).
- [24] T.H. Bui *et al.*, in *IEEE-SENSORS2015*. (Korea, 2015), pp. 323-327.
- [25] S. Chandra, M. di Marzo, Y. M. Qiao, P. Tartarini, Effect of liquid-solid contact angle on droplet evaporation. *Fire Safety Journal* **27**, 141-158 (1996).